Nanoscale

PAPER

Hafnia (HfO$_2$) nanoparticles as an X-ray contrast agent and mid-infrared biosensor

Tracie L. McGinnity,[a,c] Owen Dominguez,[b,d] Tyler E. Curtis,[a] Prakash D. Nallathamby,[a,c] Anthony J. Hoffman[b,d] and Ryan K. Roeder*[a,b,c,d]

The interaction of hafnium oxide (HfO$_2$) nanoparticles (NPs) with X-ray and mid-infrared radiation was investigated to assess the potential as a multifunctional diagnostic probe for X-ray computed tomography (CT) and/or mid-infrared biosensing. HfO$_2$ NPs of controlled size were prepared by a sol−gel process and surface functionalized with polyvinylpyrrolidone, resulting in relatively spherical and monodispersed NPs with a tunable mean diameter in the range of ∼7−31 nm. The X-ray attenuation of HfO$_2$ NPs was measured over 0.5−50 mM concentration and compared with Au NPs and iodine, which are the most prominent X-ray contrast agents currently used in research and clinical diagnostic imaging, respectively. At clinical CT tube potentials >80 kVp, HfO$_2$ NPs exhibited superior or similar X-ray contrast compared to Au NPs, while both exhibited significantly greater X-ray contrast compared to iodine, due to the favorable location of the *k*-shell absorption edge for hafnium and gold. Moreover, energy-dependent differences in X-ray attenuation enabled simultaneous quantitative molecular imaging of each agent using photon-counting spectral (multi-energy) CT. HfO$_2$ NPs also exhibited a strong mid-infrared absorption in the Reststrahlen band from ∼250−800 cm^{-1} and negative permittivity below 695 cm^{-1}, which can enable development of mid-infrared biosensors and contrast agents, leveraging surface enhanced mid-infrared and/or phonon polariton absorption.
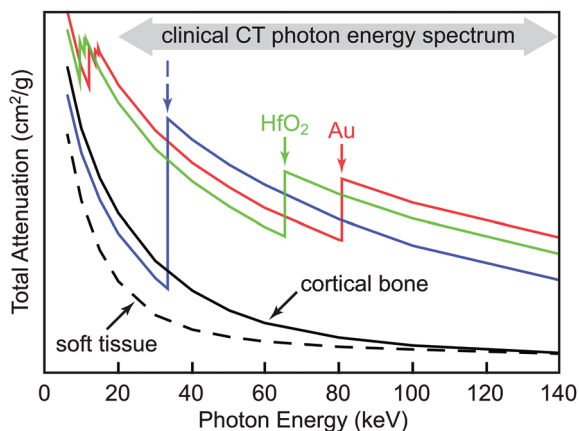
[a]Department of Aerospace and Mechanical Engineering, Bioengineering Graduate Program, University of Notre Dame, Notre Dame, IN 46556, USA.
E-mail: rroeder@nd.edu; Tel: +1 (574) 631-7003
[b]Department of Electrical Engineering, University of Notre Dame, Notre Dame, IN 46556, USA
[c]Harper Cancer Research Institute, University of Notre Dame, Notre Dame, IN 46556, USA
[d]Notre Dame Center for Nanoscience and Nanotechnology (NDnano), University of Notre Dame, Notre Dame, IN 46556, USA

Introduction

Hafnium oxide or hafnia (HfO$_2$) nanoparticles (NPs) and thin films have been investigated for various applications including high-*k* gate dielectrics,[1,2] scintillators,[3,4] radiosensitizers,[5,6] optical waveguides[7,8] and optical coatings,[9,10] due to exhibiting a high dielectric constant (*ε* = 25), high melting point (2758 °C), high atomic number (*Z* = 72), high density (9.7 g cm^{-3}), high index of refraction, transparency to visible light (5.3−5.9 eV band gap), and chemical stability. In particular, the high atomic number and electron density of HfO$_2$ NPs promotes efficient X-ray absorption for use as a radioluminescent scintillator[3,4] or radiosensitizer in cancer radiotherapy.[5,6] Moreover, the polar crystalline structure and optical phonon energies of HfO$_2$ result in a negative permittivity in the mid-infrared enabling localized surface phonon polaritons for use as optical sensors and materials.[11,12] Therefore, HfO$_2$ NPs might also be expected to be useful as an X-ray contrast agent in computed tomography (CT) and phononic material for surface enhanced mid-infrared absorption.

NPs comprising high-*Z* metals, such as gold,[13–15] bismuth,[16,17] tantalum,[18,19] and tungsten,[20] have gained recent interest as X-ray contrast agents due to enabling the delivery of a greater mass payload compared with molecular contrast agents (*e.g.*, iodinated molecules and Gd-chelates) used clinically. Interestingly, simulations of the contrast-to-noise ratio and X-ray dose for contrast-enhanced CT with a number of prospective high-*Z* contrast agents – including iodine, gold, bismuth, gadolinium, and tungsten, among others – suggested that hafnium provided the best overall performance at clinical CT tube potentials.[21,22] The *k*-shell absorption edge of hafnium (65.4 keV) is favorably located near the mean photon energy (and highest count rate) of the photon energy spectrum in clinical CT systems, which ranges from ∼20 keV to peak tube potentials of 80–140 kVp (Fig. 1). Thus, HfO$_2$ could provide improved X-ray contrast compared with current clinical contrast agents (iodine) and a lower-cost alternative to Au NPs (0.56 USD g^{-1} Hf *vs.* 39.47 USD g^{-1} Au[23]). However, there has been no previous experimental investigation of HfO$_2$ NPs as an X-ray contrast agent.

Fig. 1 The X-ray mass attenuation coefficient of iodine (I), hafnium oxide (HfO$_2$), gold (Au), cortical bone tissue, and soft tissue *versus* photon energy showing the location of *k*-shell absorption edges for iodine, hafnium and gold at 33.2, 65.4, and 80.7 keV. X-ray mass attenuation coefficients were calculated from NIST databases.[24,25] Note that the *k*-shell absorption edge of hafnium (65.4 keV) is favorably located near the mean photon energy (and highest count rate) of the photon energy spectrum in clinical CT systems, which ranges from ~20 keV to peak tube potentials of 80–140 kVp.

Noble metal NPs are able to scatter and absorb visible and infrared frequencies of light, enabling photonic and biophotonic applications in these frequency ranges.[26–28] Optical applications can benefit from using mid-infrared wavelengths because many molecules exhibit strong, characteristic absorption at these wavelengths. Coupling the benefits of strong and specific mid-infrared absorption with nanomaterials is promising for a new generation of photonic and biophotonic devices and applications, including biosensors and single molecule spectroscopy. However, the large permittivity of noble metal NPs, limits utility beyond the near-infrared. The excitation of surface phonon polariton modes in polar dielectrics enables applications in the mid-infrared that are analogous to plasmonic applications.[11,12] The permittivity of HfO$_2$ NPs is negative in the mid-infrared between the longitudinal and transverse optical phonon wavelengths,[29] allowing excitation of sub-diffraction surface phonon polariton modes that are similar to those used in plasmonics, but at mid-infrared frequencies. Thus, HfO$_2$ NPs could play an important role in the development of mid-infrared sensors based on surface enhanced mid-infrared absorption or phonon polariton absorption, and as contrast agents for mid-infrared imaging.

Therefore, the objective of this study was to investigate the interaction of HfO$_2$ NPs with X-ray and mid-infrared radiation to assess potential as a multifunctional diagnostic probe for X-ray CT and mid-infrared biosensing, respectively. HfO$_2$ NPs of controlled size were prepared by a sol–gel process and surface functionalized to promote colloidal stability. The X-ray attenuation of HfO$_2$ NPs was measured and compared with Au NPs and iodine (iohexol) over a range of concentrations and X-ray tube potentials. Mid- to far-infrared transmission spectra

were measured for HfO$_2$ NPs and fit using a Lorentz multiple oscillator model to estimate the permittivity.

Results and discussion

HfO$_2$ NP synthesis, surface modification, and characterization

HfO$_2$ NPs of controlled size were prepared by a sol–gel process, calcining a polymerized complex at 500, 575, 650, 800, and 950 °C. The crystallographic phase and crystallite size was characterized by X-ray diffraction (XRD). All XRD peaks corresponded to monoclinic HfO$_2$ (JCPDS 34-0104)[30] with no evidence of second phases at the calcination temperatures investigated (Fig. 2). The crystallite size measured by XRD peak broadening increased with increased calcination temperature (Table 1), as expected due to particle growth. However, transmission electron microscopy (TEM) revealed that the as-prepared HfO$_2$ NPs were highly agglomerated (Fig. 3). Moreover, the hydrodynamic diameter measured by dynamic light scattering (DLS) for as-prepared HfO$_2$ NPs calcined at 575 °C was 225 (±74) nm, which reflected the presence of multi-particle agglomerates.

As-prepared HfO$_2$ NPs were dispersed by surface functionalization with polyvinylpyrrolidone (PVP) and ultrasonication. The hydrodynamic diameter measured by DLS for PVP–HfO$_2$ NPs calcined at 575 °C was 133 (±74) nm. TEM micrographs showed that PVP–HfO$_2$ NPs were spherical and well-dispersed (Fig. 4). The measured NP diameter increased with increased calcination temperature ($p < 0.0001$, ANOVA) from ~7 nm at 500 °C to ~31 nm at 950 °C, and the size distribution was relatively monodispersed (Table 1). Differences
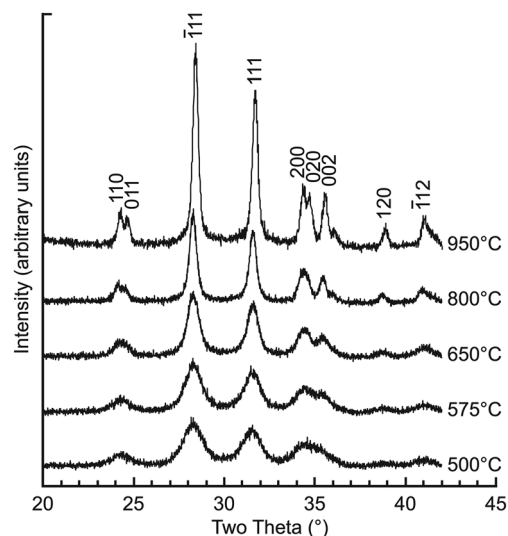
Fig. 2 Powder XRD patterns for HfO$_2$ NPs prepared from a polymerized complex at a calcination temperature of 500, 575, 650, 800, and 950 °C. All peaks correspond to monoclinic HfO$_2$ (JCPDS 34-0104).[30] The 110, 011, $\bar{1}$11, 111, 200, 020, and 002 reflections were used for crystallite size measurements (Table 1).

Table 1 The effect of calcination temperature on the size and morphology of HfO_2 NPs. The crystallite size was measured from powder XRD reflections for as-prepared HfO_2 NPs (Fig. 2). The mean (±standard deviation) NP diameter and aspect ratio were measured from TEM micrographs of PVP–HfO_2 NPs (Fig. 4). Pairwise comparisons of measurements not connected by the same superscript letter exhibited statistically significant differences between calcination temperatures ($p < 0.05$, Tukey–Kramer HSD). Differences between the mean NP size measured by XRD and TEM were not statistically significant for each calcination temperature ($p > 0.49$, t-test)

		TEM	
Temperature (°C)	XRD Crystallite size (nm)	Diameter (nm)	Aspect ratio
500	7.2 (0.8)[a]	7.4 (1.6)[a]	1.3 (0.2)[a,b]
575	8.4 (1.0)[a]	9.1 (2.3)[a]	1.3 (0.2)[a]
650	12.3 (1.0)[b]	12.5 (3.2)[b]	1.2 (0.2)[b]
800	21.2 (2.0)[c]	22.5 (5.6)[c]	1.2 (0.1)[b]
950	32.8 (1.3)[d]	31.0 (8.2)[d]	1.2 (0.1)[a,b]
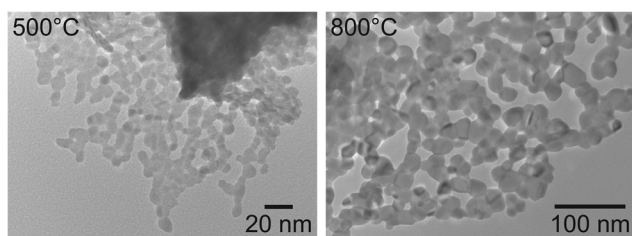
Fig. 3 Representative TEM micrographs of as-prepared HfO_2 NPs calcined at 500 and 800 °C showing highly agglomerated NPs.

between the mean NP size measured by TEM and XRD were not statistically significant for each calcination temperature ($p > 0.49$, t-test). The measured NP aspect ratio decreased slightly with increased calcination temperature ($p < 0.005$, ANOVA) from 1.3 at 500 °C to 1.2 at 950 °C (Table 1). Thus, the HfO_2 NPs were ellipsoidal, but nearly spherical, and became more spherical with increased calcination temperature.

Control of NP size and dispersion is crucial for both X-ray contrast agents and optical biosensors used either *in vivo* and *in vitro*. HfO_2 NPs have been synthesized using various hydrothermal,[31–34] solvothermal,[35,36] and sol–gel[37–39] methods. Sol–gel methods are advantageous for economical, low temperature synthesis of oxide NPs and thin films with controlled composition, size, and morphology. Previous studies for sol–gel derived HfO_2 NPs investigated reactant and surfactant concentrations,[37–39] but, surprisingly, had not investigated the ability to tune the NP size *via* the calcination temperature. The results of the present study showed an ability to tailor the HfO_2 NP size over a four-fold range of ~7–31 nm at 500–950 °C (Table 1). Importantly, NPs in this size range are suitable for *in vitro* labeling, *in vivo* delivery and cellular internalization.[15,40,41] Sol–gel derived HfO_2 NPs were previously surface modified by chemisorption of oleic acid to create hydrophobic instead of hydrophilic surfaces,[38,42] but these studies appear to be the only that have investigated surface modification. The results of the present study showed that PVP served as an effective non-ionic, steric dispersant for HfO_2 NPs.

X-ray contrast

The X-ray attenuation of HfO_2 NPs calcined at 575 °C and surface functionalized with PVP was compared with Au NPs and iodine (iohexol). Au NPs have become the most prominent NP X-ray contrast agent used in research and iodine is the most prominent X-ray contrast agent used in clinical diagnostic imaging.[13–15] Imaging phantoms were prepared comprising HfO_2 NPs, Au NPs, and iodine at concentrations ranging from 0.5 to 50 mM, as well as air and water controls for internal calibration of linear attenuation coefficients to Hounsfield units (HU). Each composition and concentration was dispersed in 1% agarose to maintain homogeneity and stability for imaging by multiple CT instruments over a period of months.

The phantoms were first imaged using a conventional laboratory micro-CT (Scanco μCT-80) operating at relatively low tube potentials (45 and 70 kVp) and high spatial resolution
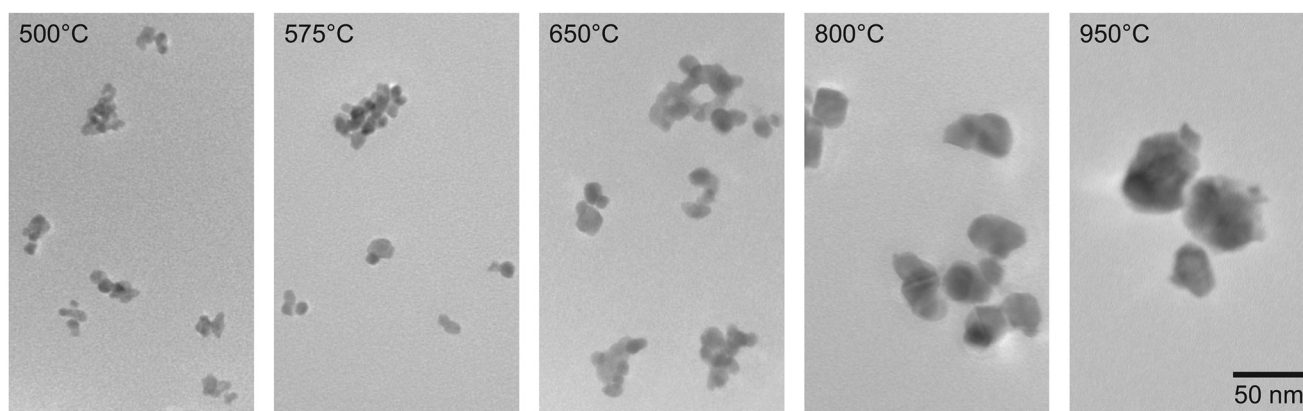
Fig. 4 Representative TEM micrographs of HfO_2 NPs calcined at 500, 575, 650, 800, and 950 °C after surface functionalization with PVP showing dispersed NPs and increased NP size with increased calcination temperature. NP size and morphology measurements are shown in Table 1.
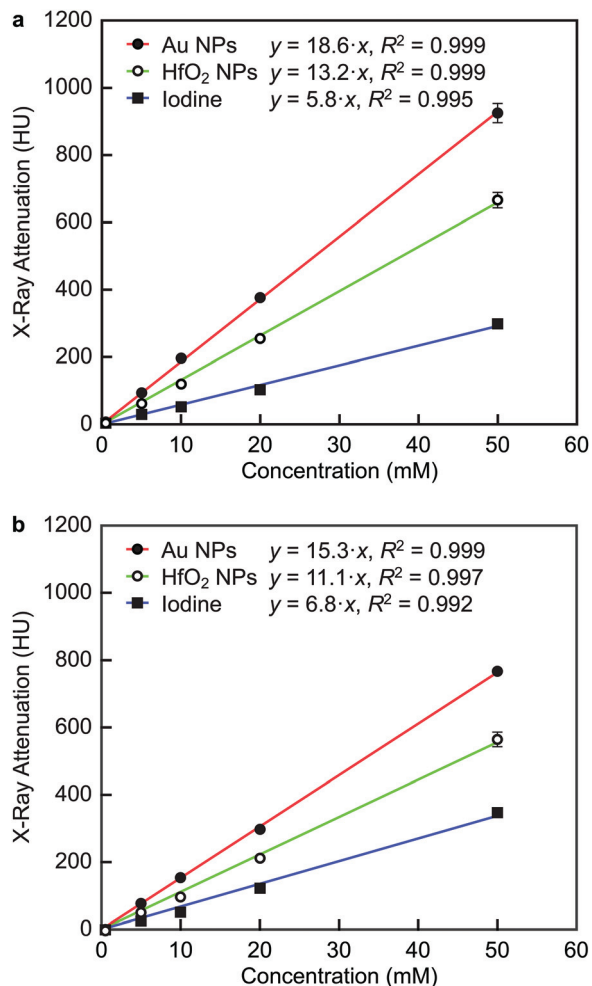
Fig. 5 The X-ray attenuation (HU) measured by micro-CT (Scanco μCT-80) at (a) 45 kVp and (b) 70 kVp for HfO_2 NPs, Au NPs, and iodine (iohexol) at concentrations ranging from 0.5 to 50 mM. Error bars show one standard deviation of the mean for three replicates. Error bars not shown lie within the data point. The effects of the group (composition), covariate (concentration), and interaction (slope) were all statistically significant at each tube potential ($p > 0.0001$, ANCOVA). The measured X-ray attenuation rate (slope, HU mM^{-1}) of HfO_2 NPs was greater than iodine but less than Au NPs ($p < 0.0005$, ANCOVA) at either tube potential.
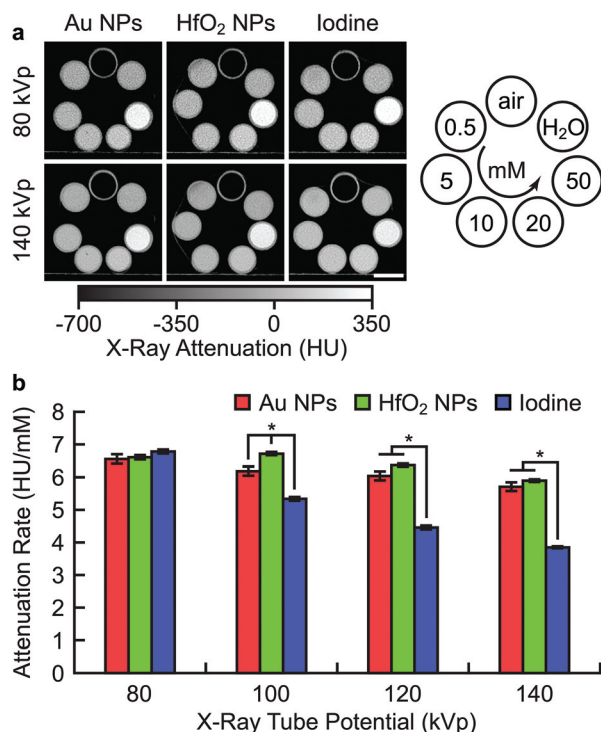
(10 μm). The X-ray attenuation of HfO_2 NPs, Au NPs, and iodine increased linearly with molar concentration ($p < 0.0001$, $R^2 > 0.99$), as expected (Fig. 5). The effects of the group (composition), covariate (concentration), and interaction (slope) were all statistically significant at each tube potential ($p > 0.0001$, ANCOVA). The measured X-ray attenuation rate (slope, HU mM^{-1}) of HfO_2 NPs was greater than iodine, but less than Au NPs ($p < 0.0005$, ANCOVA) at either tube potential (Fig. 5). HfO_2 and Au NPs exhibited a greater X-ray attenuation rate at 45 kVp compared to 70 kVp ($p < 0.0001$, ANCOVA), while iodine exhibited lower X-ray attenuation at 45 kVp compared to 70 kVp ($p < 0.0001$, ANCOVA) (Fig. 5).

X-ray attenuation increases linearly with increased mass or molar concentration of a contrast agent or any material, and is

not affected by NP size.[43] Therefore, the X-ray attenuation of different contrast agents can be directly compared at equal concentration or as an attenuation rate (HU mM^{-1}),[14,15] as reported in Fig. 5. Both HfO_2 and Au NPs exhibited significantly improved X-ray contrast compared to iodine, and Au NPs exhibited significantly greater contrast compared to HfO_2 at the relatively low tube potentials (45 and 70 kVp) used in the laboratory micro-CT. However, X-ray attenuation also increases with decreased incident photon energy from the X-ray source for any material, unless an absorption edge is encountered for that material, due to a greater probability of photoelectric absorption with decreased photon penetration.[25,44] The incident X-ray photon energy spectrum is controlled by setting the peak tube potential (kVp), which corresponds to the maximum photon energy in the spectrum, and beam filtration, which removes low energy photons (<15 keV), such that the mean photon energy is typically ~30–40% of peak tube potential. Iodine, hafnium, and gold exhibit a k-shell absorption edge at 33.2, 65.4, and 80.7 keV, respectively.[45] Therefore, the X-ray attenuation of HfO_2 and Au NPs decreased with increased tube potential (Fig. 5), due to little or no influence of the k-edges at photon energies less than 70 keV (Fig. 1). In contrast, the X-ray attenuation of iodine increased slightly with increased tube potential (Fig. 5), due to a greater number of high energy photons above the k-edge of iodine at 33.2 keV (Fig. 1). Importantly, the relatively low tube potentials (45 and 70 kVp) used in laboratory micro-CT systems produce a mean photon energy which is well below, and thus not optimal for leveraging, the k-edge of hafnium relative to gold and iodine. Thus, laboratory micro-CT systems do not reflect relative differences in the X-ray attenuation of the contrast agents when imaging higher tube potentials used clinically.

The same phantoms were, therefore, also imaged using a conventional clinical CT (Siemens SOMATOM Definition Flash) operating in single-source mode at higher tube potentials (80, 100, 120, and 140 kVp) and lower spatial resolution (~300 μm). The X-ray attenuation of HfO_2 NPs, Au NPs, and iodine increased linearly with molar concentration ($p < 0.0001$, $R^2 > 0.99$), as expected. The effects of the group (composition), covariate (concentration), and interaction (slope) were all statistically significant ($p > 0.0001$, ANCOVA) at each tube potential except 80 kVp, where only the effects of the composition and concentration were statistically significant ($p > 0.005$, ANCOVA). At 80 kVp, differences in the measured X-ray attenuation rate (slope, HU mM^{-1}) between the contrast agents were not statistically significant (Fig. 6). However, at 100–140 kVp, HfO_2 and Au NPs exhibited a greater X-ray attenuation rate compared to iodine ($p < 0.005$, ANCOVA), and at 100 kVp, HfO_2 NPs exhibited a greater X-ray attenuation rate compared to Au NPs ($p < 0.005$, ANCOVA) (Fig. 6). The X-ray attenuation rate for each contrast agent decreased with increased peak tube potential ($p < 0.001$, ANCOVA), but the amount of the decrease was greatest for iodine and least for HfO_2 NPs (Fig. 6).

At tube potentials greater than 80 kVp using clinical CT, both HfO_2 and Au NPs exhibited significantly improved con-

Fig. 6 (a) Representative grayscale image slices and (b) the X-ray attenuation rate (HU mM^{-1}) measured by clinical CT (Siemens Somatom Definition Flash) at 80, 100, 120, and 140 kVp for phantoms comprising HfO$_2$ NPs, Au NPs, and iodine (iohexol) at concentrations ranging from 0.5 to 50 mM. The scale bar shows 10 mm. Error bars show one standard error from linear least-squares regression of the X-ray attenuation vs. concentration. The effects of the group (composition), covariate (concentration), and interaction (slope) were all statistically significant ($p > 0.0001$, ANCOVA) at each tube potential except 80 kVp, where only the effects of the composition and concentration were statistically significant ($p > 0.005$, ANCOVA). Asterisks show statistically significant differences between contrast agents at a given tube potential ($p < 0.005$, ANCOVA).

trast compared to iodine (Fig. 6). The greater X-ray attenuation of both HfO$_2$ and Au NPs compared to iodine at clinical tube potentials was due to the presence of a k-shell absorption edge for hafnium and gold at 65.4 and 80.7 keV, respectively, which affects a greater proportion of incident photons at higher tube potentials (Fig. 1). The improved contrast of Au NPs compared to iodine was previously reported and attributed to this same effect.[14] However, in the present study, we report the first data showing superior contrast from HfO$_2$ compared to Au NPs at 100 kVp, and comparable contrast at 80, 120, 140 kVp (Fig. 6). The greater X-ray attenuation of HfO$_2$ compared to Au NPs was also due to the favorable location of the k-shell absorption edge for hafnium compared to the mean photon energy (and highest count rate) of the photon energy spectrum in clinical CT systems, which ranges from ~20 keV to peak tube potentials of 80–140 kVp (Fig. 1). This potential advantage of hafnium at clinical CT tube potentials was previously predicted by simulations[21,22] and measured for hafnium chloride solutions,[22] but was demonstrated in this study using HfO$_2$ NPs. Thus, the results of this study suggest that HfO$_2$ NPs may

provide a lower cost alternative to Au NPs as an X-ray contrast agent which also outperforms iodine and performs comparably, if not advantageously, to Au NPs. Furthermore, energy-dependent differences in the X-ray attenuation of contrast agents can also enable multi-agent imaging using nascent spectral CT imaging methods.[46,47]

The same phantoms were, therefore, also imaged using a novel preclinical spectral CT (MARS Bioimaging) operating at 120 kVp and ~300 μm spatial resolution, but utilizing a photon-counting detector (Medipix3RX)[48] to enable multi-energy imaging.[49] Energy bins were set to 7.0–14.8, 14.8–33.1, 33.1–65.0, 65.0–80.1, and 80.1–120 keV in order to leverage the k-shell absorption edge of iodine (33.2 keV), hafnium (65.4 keV), and gold (80.7 keV). An excised rabbit femur was also embedded in agarose as an additional control to demonstrate the decomposition of the contrast agents versus bone.

Spectral CT enabled simultaneous color delineation and quantitative molecular imaging of the HfO$_2$ NPs, Au NPs, and iodine contrast agents at 50 mM concentration, which is not possible using conventional CT due to relatively similar overall attenuation (Fig. 7). Thus, multi-energy imaging within the five selected energy bins enabled multi-agent or multi-material imaging due to differences in the energy-dependent X-ray attenuation of each material (Fig. 1). The contrast agents were also able to be clearly distinguished from bone and water, although there was a small amount of erroneous gold signal immediately adjacent to the bone likely due to beam hardening (Fig. 7). Note that a Au NP concentration of 50 mM can be readily achieved by targeted delivery and has been widely reported to be nontoxic, suggesting that these concentrations are suitable for in vivo preclinical imaging.[15] Thus, novel contrast agents like HfO$_2$ NPs and spectral CT may act synergistically to transform CT into a molecular imaging modality.

The combined results using a laboratory micro-CT, clinical CT, and novel photon-counting spectral CT suggest that HfO$_2$ NPs have considerable potential as an X-ray contrast agent. However, future work must investigate surface functionalization strategies for biostability and active targeting, as well as cytocompatibility. An in vitro toxicological assessment of industrial HfO$_2$ NPs concluded that HfO$_2$ NPs are relatively non-toxic to living cells.[50] An evaluation of the cytotoxicity of the HfO$_2$ NPs prepared in this study is currently underway. Importantly, the utility of HfO$_2$ NPs is not limited to X-ray contrast, but also includes strong mid-infrared absorption for potential photonic biosensing.

Optical properties

Transmission spectra of as-prepared HfO$_2$ NPs calcined at 575 °C were measured under vacuum from the far- (red curve) to mid-infrared (blue curve) using FTIR (Fig. 8a). The NPs were sandwiched between two 2.5 μm-thick Mylar films for wideband measurements; therefore, the transmission spectrum of the Mylar films is shown for comparison in the inset and the absorption bands characteristic of polyethylene terephthalate (Mylar) are indicated by gray shading. The HfO$_2$ NP spectra was obtained by dividing the spectra obtained with and
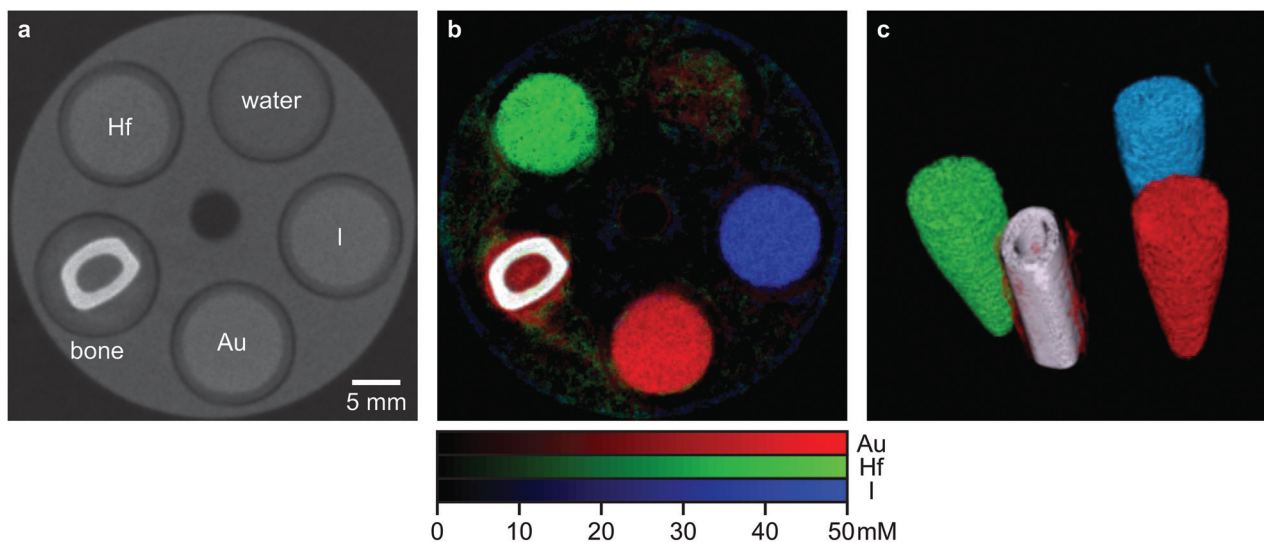
Fig. 7 Spectral CT (MARS Bioimaging) images of (clockwise from top) water, 50 mM Au NPs (red), 50 mM iodine (blue), a rabbit femur (white), and 50 mM HfO$_2$ NPs (green). (a) A representative 2D grayscale image slice showing the inability of a conventional CT image to distinguish NP compositions, and the greater signal of bone compared to 50 mM concentrations. (b) A representative 2D spectral CT image slice showing clear, color delineation and quantitative molecular imaging of the contrast agent compositions at 50 mM concentration *versus* bone and water. (c) A 3D spectral CT reconstruction showing NP compositions *versus* bone.

without NPs to remove absorption from the thin Mylar films. Nonetheless, some artifacts remained in the NP spectra due to strong absorption in the thin films and are shown by gray shading (Fig. 8a). Importantly, the low transmittance from ~250 to 800 cm^{-1} was due to strong optical absorption in the *Reststrahlen* band of HfO$_2$ (Fig. 8a). In this spectral region, the permittivity of the NPs can be negative.

The mid-infrared transmission spectra of HfO$_2$ NPs was also measured by sandwiching NPs between two KBr windows to enable the observation of absorptions due to optical phonon modes. HfO$_2$ NPs exhibited five minima in the transmission spectra at 421, 521, 596, 679, and 766 cm^{-1} (Fig. 8b). The transmission spectrum was fit using a multiple-oscillator model (dashed red curve),[29] which showed good agreement between the model and experimental data (Fig. 8b). The fit parameters were also in agreement with FTIR measurements of monoclinic HfO$_2$ thin films and density functional perturbation theory calculations.[29,51] The permittivity of HfO$_2$ NPs was subsequently determined using the multiple-oscillator model (Fig. 8b, inset) and was negative below 695 cm^{-1} (14.4 μm). Therefore, HfO$_2$ NPs were predicted to support local surface phonon polariton modes (Re(ε) ≈ −2) at several frequencies, which may be useful for optical biosensing applications leveraging surface enhanced mid-infrared or phonon polariton absorption.[11]

Conclusions

HfO$_2$ NPs exhibited strong absorption of X-ray and mid-infrared radiation suggesting utility as a multifunctional diagnostic probe for X-ray CT and/or mid-infrared biosensing. Spherical and monodispersed HfO$_2$ NPs with a tunable mean diameter

in the range of ~7–31 nm, which is suitable for *in vitro* labeling and *in vivo* delivery, were prepared by a sol–gel process, calcining a polymerized complex at 500–950 °C, and were surface functionalized with polyvinylpyrrolidone. The X-ray attenuation (HU) of HfO$_2$ NPs was measured over 0.5–50 mM concentration and compared with Au NPs and iodine, which are the most prominent X-ray contrast agents currently used in research and clinical diagnostic imaging, respectively. In a laboratory micro-CT operating at relatively low tube potentials (<80 kVp), both HfO$_2$ and Au NPs exhibited significantly greater contrast (HU mM^{-1}) compared to iodine, and Au NPs also exhibited significantly greater contrast compared to HfO$_2$, but the relatively low tube potentials used in a laboratory micro-CT did not take advantage of the *k*-edge of hafnium and were not reflective of clinical CT. In a clinical CT operating at higher tube potentials (>80 kVp,) HfO$_2$ NPs exhibited superior or similar contrast compared to Au NPs, while both exhibited significantly greater contrast compared to iodine, due to the favorable location of the *k*-shell absorption edge for hafnium and to a lesser extent gold. Therefore, HfO$_2$ NPs offer an alternative to Au NPs as an X-ray contrast agent which also outperforms iodine and performs comparably, if not advantageously, to Au NPs. Additionally, in a novel spectral CT operating at 120 kVp and utilizing a photon-counting detector, multi-energy imaging enabled simultaneous quantitative molecular imaging of HfO$_2$ NPs, Au NPs, and iodine due to energy-dependent differences in the X-ray attenuation of each agent. HfO$_2$ NPs also exhibited a strong mid-infrared absorption in the *Reststrahlen* band from ~250 to 800 cm^{-1} and negative permittivity below 695 cm^{-1}, which can support localized surface phonon polariton modes at several frequencies. Therefore, HfO$_2$ NPs may also enable development of mid-infrared
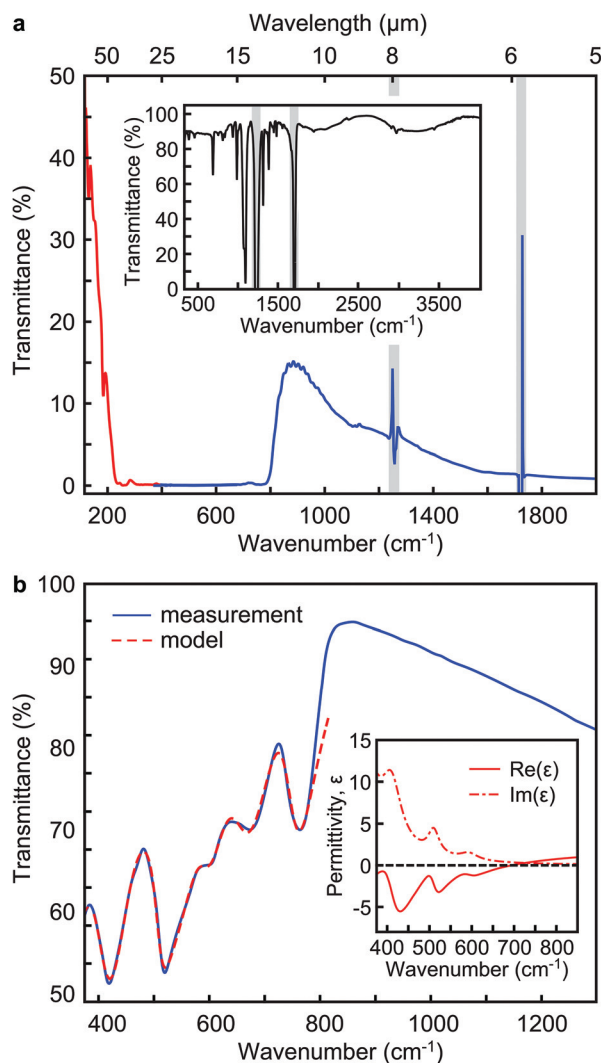
Fig. 8 (a) Far- (red) and mid-infrared (blue) transmission spectrum for ~22.5 nm HfO$_2$ NPs between two thin (2.5 μm) Mylar films. The inset shows the measured transmission spectrum for the Mylar films without NPs and the gray shading indicates regions of strong absorption that cause artifacts in the NP transmission spectrum. The low transmittance from ~250 to 800 cm^{-1} is due to strong optical absorption in the *Reststrahlen* band of HfO$_2$, where the permittivity can be negative. (b) A portion of the measured mid-infrared transmission spectrum for HfO$_2$ NPs between two KBr windows showing the measured spectrum (blue) and the best fit calculated by nonlinear least squares regression (dashed red). The inset shows the real (solid red) and imaginary (dot-dash red) parts of the multiple-oscillator permittivity extracted *via* the fitting process.

biosensors and contrast agents, leveraging surface enhanced mid-infrared and/or phonon polariton absorption.

Experimental methods

HfO$_2$ nanoparticle (NP) synthesis and surface modification

HfO$_2$ NPs were prepared by a sol–gel process using a polymerized complex, adapting previously established methods.[38]

Aqueous reaction solutions were prepared by adding 0.208 M hafnium(IV) chloride, HfCl$_4$ (99.9%, Alfa Aesar, Ward Hill, MA), to 24 mL of 2.08 M citric acid (ACS reagent, Fisher Scientific, Pittsburgh, PA) and stirring overnight to ensure complete dissolution. 0.2 M ethylene glycol (ACS reagent, BDH Chemicals, Radnor, PA) was added to the solution under continuous stirring for 3 h at 90 °C to boil off excess water. The resulting gel was subsequently calcined for 2 h in a preheated furnace at 500, 575, 650, 800, and 950 °C to pyrolyze the remaining organics and crystallize HfO$_2$ NPs. The resulting HfO$_2$ powder was ground using a mortar and pestle prior to further preparations and characterization. As-prepared HfO$_2$ NPs were surface functionalized by adding 1 wt% polyvinylpyrrolidone (PVP, M_w = 40 000, Sigma-Aldrich, St Louis, MO) to solutions containing 50–100 mM HfO$_2$ NPs and stirring overnight.

X-ray diffraction (XRD)

The crystallographic phase and crystallite size of as-prepared HfO$_2$ NPs was characterized by powder X-ray diffraction (XRD) (D8 Advance with Da Vinci, Bruker Corp., Madison, WI) using Cu Kα radiation generated at 40 kV and 40 mA. Powder samples were examined over 20–42° two-theta with a 0.01° step size, 2.0 s step time, and continuous sample rotation. The primary crystallite size was measured from peak broadening of the 110, 011, $\bar{1}$11, 111, 200, 020, and 002 reflections using the Scherrer equation,

$$\tau = \frac{K\lambda}{\beta \cos(\theta)}$$

where τ is the crystallite size (nm), K is a shape factor set equal to 0.9, λ is the X-ray wavelength (1.5406 nm), β is the full-width at half maximum (FWHM) peak intensity, and θ is the Bragg angle.[52] The FWHM was measured after background subtraction and peak fitting with a Pearson 7 function (OriginPro 2016, OriginLab Corp., Northampton, MA). Instrument broadening was corrected using Warren's method as,

$$\beta = \sqrt{\beta_{exp}{}^2 - \beta_{std}{}^2}$$

where β is the corrected peak broadening, β_{exp} is the measured FWHM of the HfO$_2$ NP sample, and β_{std} is the measured FWHM of a microscale HfO$_2$ powder standard (99.95% purity, Materion Advanced Chemicals Inc., Milwaukee, WI).[52] Hall–Williamson analysis[53] revealed that the effect of lattice strain was not statistically significant by least squares linear regression (JMP® 11.0, SAS Institute, Inc., Cary, NC) for each calcination temperature ($p > 0.27$); therefore, the crystallite size was measured as the mean (±standard deviation) from all XRD reflections.

Transmission electron microscopy (TEM)

TEM samples were prepared from dispersions of as-prepared HfO$_2$ NPs and PVP–HfO$_2$ NPs. As-prepared HfO$_2$ NPs were redispersed in deionized (DI) water at 25 mM. PVP–HfO$_2$ NPs were collected by centrifugation (Sorvall RC 6 Plus, Thermo Scientific, Wilmington, DE) at ~17 000g for 1 h, redispersed in

10 mL of ethanol at 5 mM, and subjected to ultrasonication (model 500, Fisher Scientific, Pittsburgh, PA) twice for 1.5 min pulsed at 40 cycles per min with a 67% duty cycle and 25% amplitude. TEM samples were prepared by pipetting a 10 μL aliquot onto a carbon-coated, copper grid (Model 01813-F, Ted Pella, Redding, CA) which was placed in an oven at 60 °C to evaporate the solvent, followed by pipetting and evaporating a second 10 μL aliquot. As-prepared and PVP–HfO$_2$ NP samples were imaged by TEM (JEOL 2011T, JEOL, Peabody, MA) at an accelerating voltage of 200 kV and a beam current of 102 mA. NP diameter and aspect ratio were calculated as the mean and ratio, respectively, of the measured prolate and equatorial particle diameter. The mean (±standard deviation) NP diameter and aspect ratio was measured for a sample of 100 NPs per experimental group.

Dynamic light scattering (DLS)

The hydrodynamic particle diameter distribution of as-prepared HfO$_2$ NPs and PVP–HfO$_2$ NPs calcined at 575 °C was measured using dynamic light scattering (DLS, Zetasizer Nano ZS90, Malvern Instruments Ltd, Worcestershire, UK). As-prepared HfO$_2$ NPs were dispersed in DI water at 5 mM concentration and allowed to settle overnight such that the stable supernatant was characterized by DLS. PVP–HfO$_2$ NPs were dispersed in DI water at 0.25 mM concentration and incubated in 2 mL of 4 M NaOH in DI water at 60 °C for 72 h followed by ultrasonication for 2 min pulsed at 35 cycles per min with a 60% duty cycle and 40% amplitude. Aliquots from this dispersion were subsequently diluted 100×, filtered (0.2 μm cellulose acetate membrane syringe filter, VWR, Radnor, PA), ultrasonicated again as described above, and characterized by DLS. The mean hydrodynamic diameter and standard deviation of the distribution were measured as the mean of three samples.

NP characterization statistical methods

Differences in the mean NP crystallite size (XRD), diameter (TEM), and aspect ratio (TEM) between calcination temperatures were compared using one-way analysis of variance (ANOVA) (JMP® 11.0). A log transform was applied to the aspect ratio data to provide a normal distribution for statistical analysis. *Post hoc* comparisons were performed using Tukey–Kramer HSD tests. Differences between the mean NP crystallite size (XRD) and diameter (TEM) at the same calcination temperature were compared using *t*-tests. The level of significance for all tests was set at $p < 0.05$.

Imaging phantom preparation

Imaging phantoms were prepared from PVP–HfO$_2$ NPs calcined at 575 °C and dispersed in DI water at 100 mM concentration by ultrasonication (model 500, Fisher Scientific, Pittsburgh, PA) for 1.5 min pulsed at 40 cycles per min with a 67% duty cycle and 20% amplitude. Serial dilutions containing 40, 20, 10, and 1 mM PVP–HfO$_2$ NPs were prepared from the 100 mM stock solution. A 2% agarose solution was prepared by dissolving agarose (molecular biology grade, Thermo

Scientific, Rockford, IL) in DI water under microwave heating for 2 min. PVP–HfO$_2$ NP solutions were mixed with the 2% agarose solution in equal parts by volume to create solutions containing 0.5, 5, 10, 20, and 50 mM PVP–HfO$_2$ NPs dispersed in 1% agarose. Three 1 mL aliquots for each concentration were pipetted into separate 1.5 mL Eppendorf tubes and solidified rapidly on ice.

Imaging phantoms were also prepared from solutions of Au NPs and iodine for comparison to HfO$_2$ NPs. Au NPs were prepared with a mean particle diameter of ∼13 nm using the citrate reduction, as described in detail elsewhere.[43] As-prepared Au NPs were surface functionalized by adding 1 wt% polyvinylpyrrolidone (PVP, M_w = 40 000, Sigma-Aldrich) to a 0.5 mM solution under stirring overnight and concentrated to a ∼100 mM stock solution by centrifugation at ∼19 000g for 1 h. A 100 mM iodine stock solution was prepared by dissolving iohexol (EP reference standard, Sigma-Aldrich) in DI water. Note that 1 mole of iohexol contains 3 moles of iodine. PVP–Au NP or iodine solutions were mixed with the 2% agarose solution in equal parts by volume to create solutions containing 0.5, 5, 10, 20, and 50 mM PVP–Au NPs or iodine dispersed in 1% agarose. Three 1 mL aliquots for each concentration were pipetted into separate 1.5 mL Eppendorf tubes and solidified rapidly on ice.

Gold concentrations in stock solutions and the accuracy of serial dilutions was verified using inductively coupled plasma-optical emission spectroscopy (ICP-OES, Optima 7000, Perkin Elmer) after digesting samples in 3% aqua regia (3 parts HCl to 1 part HNO$_3$). Calibration curves were created by diluting certified standard gold solutions (Assurance Grade, SPEX CertiPrep, Metuchen, NJ). Gold concentrations targeted by serial dilution and those measured by ICP-OES were highly correlated by linear least squares regression (R^2 = 0.999) and differences were not statistically significant ($p > 0.83$, paired *t*-test).

X-ray computed tomography (CT)

Phantoms were imaged using a laboratory micro-CT (μCT-80, Scanco Medical AG, Brüttisellen, Switzerland) with a cone beam X-ray source, 0.5 mm thick aluminum filter, and circular scan at 800 ms integration time, 10 μm isotropic resolution, and two energy levels: 45 kVp at 177 μA and 70 kVp at 113 μA. X-ray attenuation was measured for each contrast agent composition and concentration, as well as air and water control samples, within a cylindrical volume-of-interest (VOI), 0.72 cm in diameter, over 10 image slices (10 μm thickness) centered within the Eppendorf tube, corresponding to a 4.1 μL sample volume.

The same phantoms were also imaged using a clinical dual-energy CT (SOMATOM Definition Flash, Siemens, Malvern, PA) in single source acquisition mode with a cone beam X-ray source, bowtie filter, 0.4 mm tin filter, and helical scan at multiple energy levels: 80, 100, 120, and 140 kVp at an effective current of 85 mAs. Images were acquired using the inner ear ultra-high resolution (InnerEarUHR) protocol with a 512 × 512 matrix, 16 × 0.3 mm field of view, and 2 mm slice thickness. The reconstruction kernel was U75u very sharp ASA.

X-ray attenuation was measured for each contrast agent composition and concentration, as well as air and water control samples, within a cylindrical VOI, 0.32 cm in diameter, over 7 image slices (2 mm thickness) centered within the Eppendorf tube, corresponding to a 112.6 μL sample volume.

Measured linear attenuation coefficients (μ) were converted to Hounsfield units (HU) using an internal sample calibration with the mean linear attenuation coefficients measured for air (−1000 HU) and water (0 HU). The X-ray attenuation of the HfO$_2$ NPs, Au NPs, and iodine was reported in HU as the mean (±standard deviation) of three replicates for each concentration and plotted as a function of concentration. Differences between contrast agents and tube potentials were examined by comparing attenuation rates (HU mM^{-1}) calculated from linear least-squares regression (JMP® 11.0) of the measured X-ray attenuation *versus* concentration.[14,17] The effects of the contrast agent composition, concentration, X-ray tube potential, and their interactions on the measured X-ray attenuation were examined by analysis of covariance (ANCOVA) using a Bonferroni correction for multiple pairwise comparisons. The level of significance for all tests was set at $p < 0.05$. Note that the background attenuation due to agarose in the sample phantoms was negligible as the difference in linear attenuation as a function of tube potential between water and 1% agarose was not statistically significant for either the laboratory micro-CT or the clinical CT ($p > 0.50$, ANCOVA).

Photon-counting spectral X-ray CT

The same phantoms imaged by conventional X-ray CT were also imaged using a preclinical spectral CT (MARS Bioimaging Ltd, Christchurch, NZ) equipped with a photon-counting detector comprising a CdZnTe semiconductor ball-bonded to the Medipix3RX (CERN, Geneva, Switzerland) application-specific integrated circuit.[49] Images were acquired using a conventional polychromatic X-ray source (SB-120-350, Source-Ray, Inc., Ronkonkoma, NY) operating at 120 kVp and 18 μA with a 1.96 mm thick aluminum filter, and a continuous helical scan with a circular field of view 40 mm in diameter, 200 ms integration time, and 100 μm isotropic voxel size. An excised rabbit femur was also embedded in 1% agarose and imaged as an additional control sample for comparison. The photon-counting detector enabled simultaneous image acquisitions within multiple energy bins, including 7.0–14.8, 14.8–33.1, 33.1–65.0, 65.0–80.1, and 80.1–120 keV. These windows were chosen to leverage the *k*-shell absorption edge of iodine (33.2 keV), hafnium (65.4 keV), and gold (80.7 keV).[45] Quantitative material decomposition (spectral unmixing) was performed using a quadratic programming algorithm[54] in Matlab (v8.5, Mathworks, Natick, MA) which was calibrated by the measured X-ray attenuation of 50 mM NP concentrations, a bone mimicking composition containing 40 vol% hydroxyapatite,[55] acrylic plastic, 1% agarose, and water. The fractional abundance of gold, hafnium, and iodine were then assigned to RGB channels, respectively, and scaled to mM concentrations. 2D image slices and 3D reconstructions were produced using MARSvision software (MARS Bioimaging Ltd).

Fourier transform infrared (FTIR) spectroscopy

The transmission spectra of as-prepared HfO$_2$ NPs calcined at 575 °C were characterized under vacuum by FTIR (Vertex 80v, Bruker Corp., Billerica, MA). Room-temperature DLaTGS detectors with mid-infrared and far-infrared transparent windows were used with KBr and Mylar beamsplitters to measure spectra in the mid- and far-infrared, respectively. HfO$_2$ NPs were sandwiched between 2.5 μm thick Mylar films and KBr windows for broadband and mid-IR measurements, respectively. The average of 1000 collected spectra was reported using 4 cm^{-1} spectral resolution. The background was measured and accounted in the transmittance results.

The mid-infrared transmission spectra measured using the KBr windows were numerically fit *via* a nonlinear least-squares process using a multiple-oscillator model for the frequency-dependent permittivity and transfer matrix code to simulate the transmission. The permittivity is given by,

$$\varepsilon(\nu) = A^2 + C\nu^2 + \sum_k \frac{\nu_{pk}{}^2}{\nu_k{}^2 + \nu^2 - i\gamma_k\nu}$$

where ε is the permittivity, A and C are constants from the Cauchy formula, ν is frequency, ν_{pk} is the plasma frequency, ν_k is the resonance frequency, γ_{pk} is the dampening coefficient, and k is the phonon mode.[29]

Acknowledgements

References

1 Y. Aoki, T. Kunitake and A. Nakao, Sol-gel fabrication of dielectric HfO$_2$ nano-films; formation of uniform, void-free layers and their superior electrical properties, *Chem. Mater.*, 2005, **17**, 450–458.

2 L. Armelao, H. Bertagnolli, D. Bleiner, M. Groenewolt, S. Gross, V. Krishnan, C. Sada, U. Schubert, E. Tondello and A. Zattin, Highly dispersed mixed zirconia and hafnia nanoparticles in a silica matrix: First example of a ZrO$_2$-HfO$_2$-SiO$_2$ ternary oxide system, *Adv. Funct. Mater.*, 2007, **17**, 1671–1681.

3 C. LeLuyer, M. Villanueva-Ibaflez, A. Pillonnet and C. Dujardin, HfO$_2$:X (X=Eu^{3+}, Ce^{3+}, Y^{3+}) sol gel powders for

ultradense scintillating materials, *J. Phys. Chem. A*, 2008, **112**, 10152–10155.

4 C. Liu, T. J. Hajagos, D. Kishpaugh, Y. Jin, W. Hu, Q. Chen and Q. Pei, Facile single-precursor synthesis and surface modification of hafnium oxide nanoparticles for nanocomposite γ-ray scintillators, *Adv. Funct. Mater.*, 2015, **25**, 4607–4616.

5 L. Maggiorella, G. Barouch, C. Devaux, A. Pottier, E. Deutsch, J. Bourhis, E. Borghi and L. Levy, Nanoscale radiotherapy with hafnium oxide nanoparticles, *Future Oncol.*, 2012, **8**, 1167–1181.

6 J. Marill, N. M. Anesary, P. Zhang, S. Vivet, E. Borghi and L. Levy, Hafnium oxide nanoparticles: Toward an in vitro predictive biological effect?, *Radiat. Oncol.*, 2015, **9**, 150 (11 pages).

7 S. J. L. Ribeiro, Y. Messaddeq, R. R. Gonçalves, M. Ferrari, M. Montagna and M. A. Aegerter, Low optical loss planar waveguides prepared in an organic–inorganic hybrid system, *Appl. Phys. Lett.*, 2000, **77**, 3502–3504.

8 R. R. Gonçalves, G. Carturan, M. Montagna, M. Ferrari, L. Zampedri, S. Pelli, G. C. Righini, S. J. L. Ribeiro and Y. Messaddeq, Erbium-activated HfO₂-based waveguides for photonics, *Opt. Mater.*, 2004, **25**, 131–139.

9 R. Chow, S. Falabella, G. E. Loomis, F. Rainer, C. J. Stolz and M. R. Kozlowski, Reactive evaporation of low-defect density hafnia, *Appl. Opt.*, 1993, **32**, 5567–5574.

10 A. J. Waldorf, J. A. Dobrowolski, B. T. Sullivan and L. M. Plante, Optical coatings deposited by reactive ion plating, *Appl. Opt.*, 1993, **32**, 5583–5593.

11 J. D. Caldwell, L. Lindsay, V. Giannini, I. Vurgaftman, T. L. Reinecke, S. A. Maier and O. J. Glembocki, Infrared and terahertz nanophotonics using surface phonon polaritons, *Nanophotonics*, 2015, **4**, 44–68.

12 K. Feng, W. Streyer, Y. Zhong, A. J. Hoffman and D. Wasserman, Photonic materials, structures and devices for *Reststrahlen* optics, *Opt. Express*, 2015, **23**, A1418–A1433.

13 J. F. Hainfeld, D. N. Slatkin, T. M. Focella and H. M. Smilowitz, Gold nanoparticles: A new X-ray contrast agent, *Brit. J. Radiol.*, 2006, **79**, 248–253.

14 M. W. Galper, M. T. Saung, V. Fuster, E. Roessl, A. Thran, R. Proksa, Z. A. Fayad and D. P. Cormode, Effect of computed tomography scanning parameters on gold nanoparticle and iodine contrast, *Invest. Radiol.*, 2012, **47**, 475–481.

15 L. E. Cole, R. D. Ross, J. Tilley, T. Vargo-Gogola and R. K. Roeder, Gold nanoparticles as contrast agents in X-ray imaging and computed tomography, *Nanomedicine*, 2015, **10**, 321–341.

16 O. Rabin, J. Manuel Perez, J. Grimm, G. Wojtkiewicz and R. Weissleder, An X-ray computed tomography imaging agent based on long-circulating bismuth sulphide nanoparticles, *Nat. Mater.*, 2006, **5**, 118–122.

17 A. L. Brown, P. C. Naha, V. Benavides-Montes, H. I. Litt, A. M. Goforth and D. P. Cormode, X-ray opacity, and biological compatibility of ultra-high payload elemental bismuth nanoparticle X-ray contrast agents, *Chem. Mater.*, 2014, **26**, 2266–2274.

18 P. J. Bonitatibus Jr., A. S. Torres, G. D. Goddard, P. F. FitzGerald and A. M. Kulkarni, Synthesis, characterization, and computed tomography imaging of a tantalum oxide nanoparticle imaging agent, *Chem. Commun.*, 2010, **46**, 8956–8958.

19 M. H. Oh, N. Lee, H. Kim, S. P. Park, Y. Piao, J. Lee, S. W. Jun, W. K. Moon, S. H. Choi and T. Hyeon, Large-scale synthesis of bioinert tantalum oxide nanoparticles for X-ray computed tomography imaging and bimodal image-guided sentinel lymph node mapping, *J. Am. Chem. Soc.*, 2011, **133**, 5508–5515.

20 A. Jakhmola, N. Anton, H. Anton, N. Messaddeq, F. Hallouard, A. Klymchenko, Y. Mely and T. F. Vandamme, Poly-ε-caprolactone tungsten oxide nanoparticles as a contrast agent for X-ray computed tomography, *Biomaterials*, 2014, **35**, 2981–2986.

21 T. Nowak, M. Hupfer, R. Brauweiler, F. Eisa and W. A. Kalender, Potential of high-Z contrast agents in clinical contrast-enhanced computed tomography, *Med. Phys.*, 2011, **38**, 6469–6482.

22 A.-C. Roessler, M. Hupfer, D. Kolditz, G. Jost, H. Pietsch and W. A. Kalender, High atomic number contrast media offer potential for radiation dose reduction in contrast-enhanced computed tomography, *Invest. Radiol.*, 2016, **51**, 249–254.

23 U.S. Geological Survey Scientific Investigations Report 2012-5188, Metal prices in the United States through 2010, U.S. Geological Survey, Reston, VA, 2013. Available at http://pubs.usgs.gov/sir/2012/5188.

24 M. J. Berger, J. H. Hubbell, S. M. Seltzer and J. Chang, *XCOM: Photon cross section database (version 1.5)*, National Institute of Standards and Technology, Gaithersburg, MD, 2010. Available at http://physics.nist.gov/xcom.

25 J. H. Hubbell and S. M. Seltzer, *Table of X-ray mass attenuation coefficients and mass energy-absorption coefficients (version 1.4)*, National Institute of Standards and Technology, Gaithersburg, MD, 2004. Available at http://physics.nist.gov/xaamdi.

26 P. K. Jain, K. S. Lee, I. H. El-Sayed and M. A. El-Sayed, Calculated absorption and scattering properties of gold nanoparticles of different size, shape, and composition: Applications in biological imaging and biomedicine, *J. Phys. Chem. B*, 2006, **110**, 7238–7248.

27 J. N. Anker, W. P. Hall, O. Lyandres, N. C. Shah, J. Zhao and R. P. Van Duyne, Biosensing with plasmonic nanosensors, *Nat. Mater.*, 2008, **7**, 442–453.

28 K. A. Willets and R. P. Van Duyne, Localized surface plasmon resonance spectroscopy and sensing, *Annu. Rev. Phys. Chem.*, 2007, **58**, 267–297.

29 T. J. Bright, J. I. Watjien, Z. M. Zhang, C. Muratore and A. A. Voevodin, Optical properties of HfO₂ thin films deposited by magnetron sputtering: From the visible to the far-infrared, *Thin Solid Films*, 2012, **520**, 6793–6802.

30 Powder Diffraction File 34-0104, HfO₂, Hafnium oxide, Joint Committee on Powder Diffraction Standards (JCPDS),

International Center for Diffraction Data (ICDD), Newton Square, PA, 2001.

31 M. Yoshimura and S. Somiya, Hydrothermal synthesis of crystallized nano-particles of rare earth-doped zirconia and hafnia, *Mater. Chem. Phys.*, 1999, **61**, 1–8.

32 P. E. Meskin, F. Y. Sharikov, V. K. Ivanov, B. R. Churagulov and Y. D. Tretyakov, Rapid formation of nanocrystalline HfO$_2$ powders from amorphous hafnium hydroxide under ultrasonically assisted hydrothermal treatment, *Mater. Chem. Phys.*, 2007, **104**, 439–443.

33 A. Sahraneshin, S. Takami, D. Hojo, K. Minami, T. Arita and T. Adschiri, Synthesis of shape-controlled and organic-hybridized hafnium oxide nanoparticles under sub- and supercritical hydrothermal conditions, *J. Supercrit. Fluids*, 2012, **62**, 190–196.

34 A. Sahraneshin, S. Asahina, T. Togashi, V. Singh, S. Takami, D. Hojo, T. Arita, K. Minami and T. Adschiri, Surfactant-assisted hydrothermal synthesis of water-dispersible hafnium oxide nanoparticles in highly alkaline media, *Cryst. Growth Des.*, 2012, **12**, 5219–5226.

35 J. Buha, D. Arčon, M. Niederberger and I. Djerdj, Solvothermal and surfactant-free synthesis of crystalline Nb$_2$O$_5$, Ta$_2$O$_5$, HfO$_2$, and co-doped HfO$_2$ nanoparticles, *Phys. Chem. Chem. Phys.*, 2010, **12**, 15537.

36 A. Lauria, I. Villa, M. Fasoli, M. Niederberger and A. Vedda, Multifunctional role of rare earth doping in optical materials: Nonaqueous sol–gel synthesis of stabilized cubic HfO$_2$ luminescent nanoparticles, *ACS Nano*, 2013, **7**, 7041–7052.

37 J. Tang, J. Fabbri, R. D. Robinson, Y. Zhu, I. P. Herman, M. L. Steigerwald and L. E. Brus, Solid-solution nanoparticles: Use of a nonhydrolytic sol–gel synthesis to prepare HfO$_2$ and Hf$_x$Zr$_{1-x}$O$_2$ nanocrystals, *Chem. Mater.*, 2004, **16**, 1336–1342.

38 R. Ramos-González, L. A. García-Cerda, H. N. Alshareef, B. E. Gnade and M. A. Quevedo-López, Study of hafnium (IV) oxide nanoparticles synthesized by polymerized complex and polymer precursor derived sol-gel methods, *Mater. Sci. Forum*, 2010, **644**, 75–78.

39 R. Ramos-González, L. A. García-Cerda and M. A. Quevedo-López, Study of the surface modification with oleic acid of nanosized HfO$_2$ synthesized by the polymerized complex derived sol–gel method, *Appl. Surf. Sci.*, 2012, **258**, 6034–6039.

40 J. H. West and N. J. Halas, Engineered nanomaterials for biophotonics applications: Improving sensing, imaging, and therapeutics, *Annu. Rev. Biomed. Eng.*, 2003, **5**, 285–292.

41 E. Oh, J. B. Delehanty, K. E. Sapsford, K. Susumu, R. Goswami, J. B. Blanco-Canosa, P. E. Dawson, J. Granek, M. Shoff, Q. Zhang, P. L. Goering, A. Huston and I. L. Medintz, Cellular uptake and fate of PEGylated gold nanoparticles is dependent on both cell-penetration peptides and particle size, *ACS Nano*, 2011, **5**, 6434–6448.

42 N. Dahal and V. Chikan, Synthesis of hafnium oxide-gold core–shell nanoparticles, *Inorg. Chem.*, 2012, **51**, 518–522.

43 R. D. Ross, L. E. Cole, J. Tilley and R. K. Roeder, Effects of functionalized gold nanoparticle size on X-ray attenuation and substrate binding affinity, *Chem. Mater.*, 2014, **26**, 1187–1194.

44 J. H. Hubbell, H. A. Gimm and I. Overbo, Pair, triplet, and total atomic cross sections (and mass attenuation coefficients) for 1 MeV-100 GeV photons in elements Z=1 to 100, *J. Phys. Chem. Ref. Data*, 1980, **9**, 1023–1147.

45 R. D. Deslattes, E. G. Kessler Jr., P. Indelicato, L. de Billy, E. Lindroth and J. Anton, X-ray transition energies: New approach to a comprehensive evaluation, *Rev. Mod. Phys.*, 2003, **75**, 35–99.

46 N. G. Anderson and A. P. Butler, Clinical applications of spectral molecular imaging: Potential and challenges, *Contrast Media Mol. Imaging*, 2014, **9**, 3–12.

47 X. Wang, D. Meier, K. Taguchi, D. J. Wagenaar, B. E. Patt and E. C. Frey, Material separation in X-ray CT with energy resolved photon-counting detectors, *Med. Phys.*, 2011, **38**, 1534–1546.

48 R. Ballabriga, M. Campbell, E. Heijne, X. Llopart, L. Tlustos and W. Wong, Medipix3: A 64 k pixel detector readout chip working in single photon counting mode with improved spectrometric performance, *Nucl. Instrum. Methods Phys. Res., Sect. A*, 2011, **633**, S15–S18.

49 M. F. Walsh, S. J. Nik, S. Procz, M. Pichotka, S. T. Bell, C. J. Bateman, R. M. N. Doesburg, N. De Ruiter, A. I. Chernoglazov, R. K. Panta, A. P. H. Butler and P. H. Butler, Spectral CT data acquisition with Medipix3.1, *J. Instrum.*, 2013, **8**, P10012.

50 J. A. Field, A. Luna-Velasco, S. A. Boitano, F. Shadman, B. D. Ratner, C. Barnes and R. Sierra-Alvarez, Cytotoxicity and physicochemical properties of hafnium oxide nanoparticles, *Chemosphere*, 2011, **84**, 1401–1407.

51 B. Zhou, H. Shi, X. D. Zhang, Q. Su and Z. Y. Jiang, The simulated vibrational spectra of HfO$_2$ polymorphs, *J. Phys. D: Appl. Phys.*, 2014, **47**, 115502.

52 B. D. Cullity, *Elements of X-Ray Diffraction*, Addison-Wesley Publishing Company, Inc., Reading, MA, 1978, pp. 284–285.

53 G. K. Williamson and W. H. Hall, X-ray line broadening from filed aluminium and wolfram, *Acta Metall.*, 1953, **1**, 22–31.

54 K. Themelis and A. A. A. Rontogiannis, A soft constrained MAP estimator for supervised hyperspectral signal unmixing, *Proc. Eur. Signal Proc. Conf. (EUSIPCO)*, Lausanne, Switzerland, 2008.

55 J. M. Deuerling, D. J. Rudy, G. L. Niebur and R. K. Roeder, Improved accuracy of cortical bone mineralization measured by polychromatic micro-computed tomography using a novel high mineral density composite calibration phantom, *Med. Phys.*, 2010, **37**, 5138–5145.